IEEE Access
Multidisciplinary | Rapid Review | Open Access Journal

Received 9 December 2024, accepted 1 January 2025, date of publication 6 January 2025, date of current version 22 January 2025.

Digital Object Identifier 10.1109/ACCESS.2025.3525760

RESEARCH ARTICLE

Active Suspension Based on a Motor-Driving Compacted Double-Gas-Chamber Hydro-Pneumatic Strut

RUIHONG LI[1], BING MA[2], FAN YANG[3,4], DEZHAO LIN[3], AND WEIQIANG ZHANG[1]

[1]Research Center for Intelligent Materials and Structures (CIMS), College of Mechanical Engineering and Automation, Huaqiao University, Xiamen, Fujian 361021, China
[2]College of Rail Transit, Henan Mechanical and Electrical Vocational College, Zhengzhou, Henan 451191, China
[3]College of Marine Engineering, Jimei University, Xiamen, Fujian 361021, China
[4]Xiamen TVS Test Science and Technology Company Ltd., Xiamen, Fujian 361021, China

Corresponding author: Fan Yang (xmyf@hotmail.com)

This work was supported in part by the National Natural Science Foundation of China (NSFC) under Grant 52401379, Grant 61733006, and Grant U1813201; and in part by Henan Province Science and Technology Research Project under Grant 242102240107.

ABSTRACT Vehicle attitude is one of the most important factors affecting ride comfort, safety, and handling, and it is influenced by road conditions, driver's maneuvers, and other factors. It is usually achieved by pumping methods (air suspension, hydro-pneumatic suspension, and so on). However, the nonlinearities, hysteresis, and uncertainties in the adjusting process caused by the gas property and the valve characteristic will increase the difficulty of controller design. And frequent use of the pump for continuous adjustment also affects the life span. This paper develops an active suspension based on Motor-driving compacted Double-gas-chamber Hydro-Pneumatic Strut (MDHPS) and verifies the possibility of attitude control with a simple PID controller. The controller is built based on the quarter-car model with the MDHPS model and the optimal values are identified through the Ziegler–Nichols method and Genetic Algorithm (GA). Finally, to investigate the attitude control effect of MDHPS, the full-car model is established based on the co-simulation of Carsim and Matlab/Simulink. The anti-roll and anti-pitch properties based on the proposed height adjustment method are evaluated under different working conditions. Through the comparison between the active and passive methods, it has been shown that the proposed method can greatly improves vehicle performance. The improvement rate of the Root Mean Square (RMS) for both roll and pitch angles exceeds 50.46% under different working conditions.

INDEX TERMS Active suspension, attitude control, Carsim-Simulink co-simulation, hydro-pneumatic strut.

I. INTRODUCTION

The vehicle attitude is essential in determining the comfort, safety, and handling of driving. It is usually influenced by various factors, including road surface conditions, driver's maneuvers, and so on [1]. Considering the increasing demands for ride comfort and handling, the attitude deflection of vehicles should be better controlled. In the vehicle structure, the suspension system is the supporting component to provide ride stability [2] and is mainly divided into passive suspension, semi-active, and active suspension. Traditional passive suspension [3], with its fixed structure, cannot be adjusted during the working process. The semi-active suspensions [4] focus on the adjustment of damping and stiffness coefficients and cannot realize the attitude control. Consequently, a number of active suspensions with different kinds of methods to achieve attitude control through height adjustment of each strut have been developed, such as the pumping method [5], [6], magnet synchronous linear motor [7], and conventional mechanical structure [8].

Pumping is the most common method to achieve height adjustment. It has been investigated by many researchers, and it is usually realized by two different approaches: air suspension [9], [10] and hydro-pneumatic suspension [11].

The associate editor coordinating the review of this manuscript and approving it for publication was Chaitanya U. Kshirsagar.

Yin et al. [12] investigated an air suspension system to adjust the stiffness and body height of the suspension system by regulating the internal air pressure through an air pump. Wang et al. [13] focused on the parameters' adjustment of hydro-pneumatic suspension under different road conditions through pumping. Considering its working principle, the pumps, solenoid valves, pressure sensors, and other complex components are required [5], which require a large space and are not conducive to compact design [14]. Besides, to achieve continuous height adjustment, a high-frequency adjustment process should be conducted, which will significantly affect the span life of the pumping system [7]. In addition, the high precision control of pumps and solenoid valves should be adopted to avoid the high impact during the adjusting process [15]. However, according to the working principle, the system's response speed is limited by the inflation and deflation process.

The adjusting of the pumping system is usually conducted by inputting or outputting the extra mass of air and/or hydraulic oil, the nonlinearities of air property and the valve characteristic will lead to uncertainties and added difficulties to the controller design in the adjusting process. It should be emphasized that as the extra mass of air and/or hydraulic oil pumping input/output the system, the total volume (gas or hydraulic oil) of the whole system cannot be constant, and then the system's dynamic properties (especially stiffness property) will change with height adjustment [16]. Therefore, advanced controllers are usually utilized in the previous research on pumping systems [16], [17]. Such as Long et al. [6] considered the hysteresis characteristic of the system due to the phenomenon of overinflation, overdeflation, and frequent inflating and deflating in electronically controlled air suspension systems. A PID control strategy with a state-preview height control strategy was established [6]; Prassad et al. [18] proposed a linear quadratic regulator (LQR) with Particle Swarm Optimization to improve the non-linear system of air suspension; Rui [19] presented an adaptive sliding-mode control method for the nonlinear dynamical characteristic of electronically controlled air suspension in the presence of parameter uncertainties; Sun et al. [20] utilized a hybrid model predictive controller (HMPC) based on online mixed-integer quadratic optimization to solve the control problem of vehicle height adjustment of electronically controlled air suspension; Zhou et al. [21] focused on cooperative control to avoid the characteristics of variable stiffness and low vibration frequency of interconnected air suspension. However, it can solve the problem of inflation by utilizing the advanced controller and high-precision solenoid valves, but the rate of deflation is still limited by the working principle.

Considering the above, the main purpose of this research paper is to develop a Motor-driving compacted Double-gas-chamber Hydro-Pneumatic Strut (MDHPS). As no extra mass of air in/out of the system, the stiffness property of the strut will be constant and/or predicted during the height adjustment procedure. Additionally, the research explores the possibility of attitude control for a full car using a simple controller. Firstly, based on the mathematic model, which has been established and verified by experimental data in the previous study, the PID controller is built based on the quarter-car model with the MDHPS model and the optimal value identified through the Ziegler–Nichols method and Genetic Algorithm (GA). And then, the established methodology was applied to a full-car model, which is established based on the co-simulation of Carsim software and Matlab/Simulink. The anti-roll and anti-pitch properties based on the proposed height adjustment method were evaluated under different working conditions, including bump excitation, acceleration, brake, and double lane-change track operation conditions. Through the comparison between the active and passive methods, it has been shown that the proposed method can greatly improves vehicle performance.

TABLE 1. The physical parameters of the mdhps prototype.

Definition	DESCRIPTION	Value
A_{MC}	Area of Main Chamber (MC)	3117.2mm^2
A_{rod}	Area of the piston rod	1590.4mm^2
A_{AC}	Area of Annular Chamber (AC)	1526.8mm^2
A_{GC}	Area of Gas Chamber (GC)	883.5mm^2
A_{SGC}	Area of Secondary Gas Chamber (SGC)	3117.2mm^2
A_{AGC}	Area of Adjustable Gas Chamber (AGC)	1256.6mm^2
ρ	Density of the oil	797kg/m^3
C_d	Flow coefficient	0.7
n_{13}	Number of orifices between MC and AC	2
a_{13}	Area of orifice between the MC and AC	8.04mm^2
V_{GC0}	Maximum volume of GC	224000mm^3
V_{SGC0}	Maximum volume of SGC and AGC	385000mm^3
h_{b0}	Maximum length of h_b	104mm

II. STRUCTURE AND WORKING PRINCIPLE

In this section, the working principle associated with the structure design of the proposed Motor-driving compacted Double-gas-chamber Hydro-Pneumatic Strut (MDHPS) is introduced. The prototype and experimental platform of MDHPS are illustrated in Figure. 1. The proposed MDHPS consists of two parts: Main body and Driving part. The Main body includes Gas Chamber (GC), Secondary Gas Chamber (SGC), and Adjustable Gas Chamber (AGC), which are all filled with nitrogen. Since the gas volume of SGC and AGC are connected, the change of AGC volume achieved by the movement of Regulating Piston (RP) driven by the stepper motor through the ball screw (Driving part), will affect the volume/pressure distribution in the Main body, and then the suspension strut height (H). The internal of the piston rod is connected to the Main Chamber (MC), allowing the oil to flow freely between these two chambers. The designed parameters of the MDHPS prototype are listed in Table 1.

III. ESTABLISHMENT OF THE MATHEMATICAL MODEL

A. FUNDAMENTAL MODEL OF THE PROPOSED MDHPS SYSTEM

As the detailed modelling procedure and its function has been established and verified in the previous study, for the sake

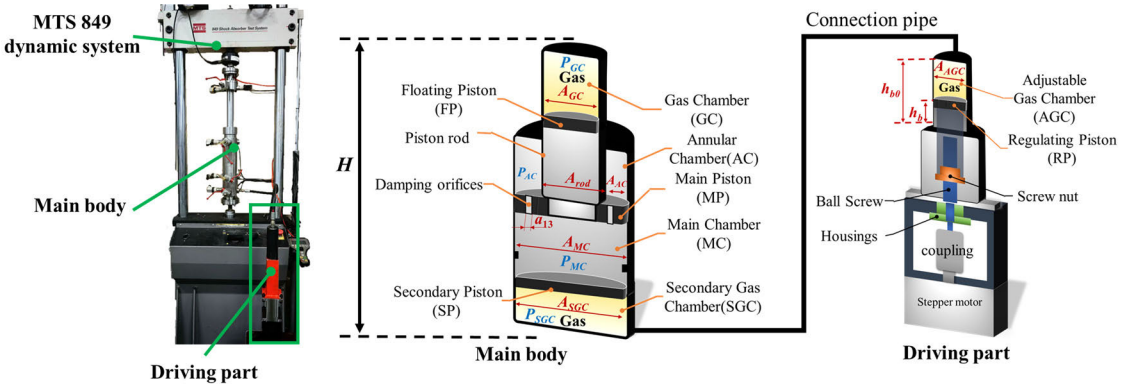

FIGURE 1. The experimental platform and schematic of the proposed MDHPS.

of the article's completeness, the key modelling steps (parts) will be summarized based on reference [22] in this section. The output force of the MDHPS can be expressed as:

$$F = P_{MC} \cdot A_{MC} - P_{AC} \cdot A_{AC} + f_{PR} \cdot sign(\dot{x}) \tag{1}$$

where P_{MC} and P_{AC} represent the pressure of Main Chamber (MC) and Annular Chamber (AC), respectively; A_{MC} and A_{AC} represent the area of MC and AC, respectively; f_{PR} represents the friction, as shown in Figure. 1; $\dot{x}$ represents the velocity of Main Piston (MP). From Eq. (1), it can be found that the output force consists of three parts as:

1) SPRING FORCE

Based on the ideal gas law, the gas pressure can be expressed as [23]:

$$(P_{i0} + P_a) \cdot V_{i0}^n = (P_i + P_a) \cdot V_i^n; (i = GC \ or \ SGC) \tag{2}$$

where P_{i0} and P_i represent the initial and working pressure of i chamber, respectively; P_a represents the atmospheric pressure (0.1MPa); V_{i0} and V_i represent the initial and working volume of i chamber, respectively; n represents the polytropic exponent ($n = 1.2$ [22], [24], [25]). The volume of the GC (V_{GC}) and the sum volume of SGC and AGC (V_{SGC}) can be calculated as:

$$V_{GC} = V_{GC0} - A_{GC} \cdot x_{FP} \tag{3}$$

$$V_{SGC} = V_{SGC0} - A_{SGC} \cdot x_{SP} - A_{AGC} \cdot h_b \tag{4}$$

where A_{GC} represents the cross-sectional area of GC; x_{FP} represents the displacement of Floating Piston (FP); A_{SGC} and A_{AGC} represent the cross-sectional area of SGC and AGC, respectively; x_{SP} represents the displacement of Secondary Piston (SP), respectively. The direction of movement of the pistons during compression is defined as the positive direction. The relation between compression displacement (x) of the MP, x_{FP} and x_{SP} can be calculated as:

$$A_{MC} \cdot x = A_{GC} \cdot x_{FP} + A_{SGC} \cdot x_{SP} \tag{5}$$

2) OIL DAMPING FORCE

The oil damping force can be expressed as [26]:

$$|P_{MC} - P_{AC}| = (q_{13}^2 \cdot \rho) \Big/ [2 \cdot (C_d \cdot n_3 \cdot a_3)^2] \tag{6}$$

where P_{MC} and P_{AC} represent the pressure of MC and AC, respectively; C_d represents the flow coefficient (C_d =0.7 [27]); n_3 and a_3 represent the number and cross-sectional area of damping orifices, respectively; q_{13} represents the flow from MC to AC, which can be expressed as:

$$q_{13} = q_1 - q_{12} = A_{MC} \cdot (\dot{x} - \dot{x}_{SP}) - A_{GC} \cdot \dot{x}_{FP} \tag{7}$$

where q_1 represents the flow out of MC; q_{12} represents the flow from MC to the inside of the piston rod; $\dot{x}_{SP}$ and $\dot{x}_{FP}$ represent the velocity of SP and FP, respectively.

3) FRICTION FORCE

The friction force (f_{PR}), which can be described by the continuous zero-velocity crossing friction model as [28]:

$$f_{PR} = -\mu_k \cdot F_c \cdot c_l \cdot \frac{\dot{x}}{|\dot{x}|} \tag{8}$$

$$c_l = \begin{cases} 0 & |\dot{x}| \le v_0 \\ (\dot{x} - v_0) \big/ (v_l - v_0) & v_0 \le |\dot{x}| \le v_l \\ 1 & |\dot{x}| \ge v_l \end{cases} \tag{9}$$

where μ_k represents the coefficient of kinetic friction and is set to 0.1 [28]; F_c represents the normal reaction force; v_0 and v_l are the given tolerances for the velocity. The floating pistons' friction is ignored in this paper. The gas/oil pressure in MDHPS can be expressed as:

$$P_{GC} = P_{MC} = P_{AGC} \tag{10}$$

where P_{GC}, P_{AGC}, and P_{MC} represent the pressure in GC, AGC, and MC, respectively. The parameters of the friction force between the piston rod and the cylinder can be calculated through Eq. (1). According to the experimental data, the parameters of the friction model are set as: $F_c = 1000$, $v_l = 0.1$, and $v_0 = 0$. The main purpose of this paper is to develop an active suspension based on Motor-driving compacted

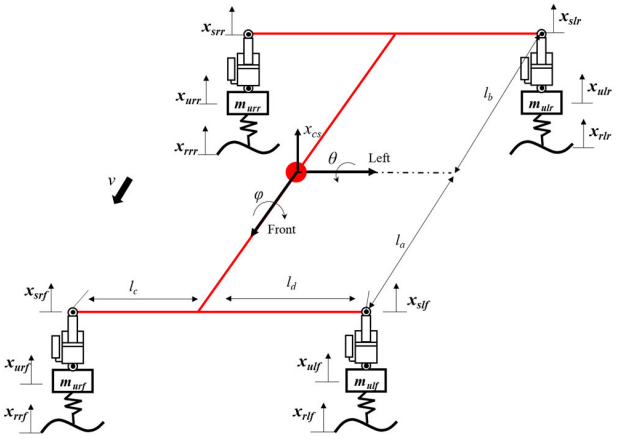

FIGURE 2. The schematic diagram of the seven-degree-of-freedom full-car model.

TABLE 2. Structural parameter values of full car model.

Parameter	DEFINED	Value
l_a	Distance between front axle and vehicle center of mass	1.015m
l_b	Distance between rear axle and vehicle center of mass	1.895m
l_c	Distance between left axle and vehicle center of mass	0.8375m
l_d	Distance between right axle and vehicle center of mass	0.8375m
m_{s_full}	Sprung mass of the full car	1270 kg
m_{ulf}, m_{urf}	Unsprung mass of left and right front suspension, respectively	88.6 kg
m_{ulr}, m_{urr}	Unsprung mass of left and right rear suspension, respectively	54.4 kg
I_{lr}	Roll inertia	536.6kg·m^2
I_{fr}	Pitch inertia	1536.7kg·m^2
k_{ulr}, k_{urr}	Front axle tire stiffness	268N/mm
k_{ulf}, k_{urf}	Rear axle tire stiffness	268N/mm

Double-gas-chamber Hydro-Pneumatic Strut (MDHPS) and to verify the feasibility of attitude control with a simple PID controller. The established model has been validated in the previous research [29]. For the sake of clarity, the verification process is omitted in this paper.

B. SEVEN-DEGREE-OF-FREEDOM FULL-CAR MODEL

The schematic diagram of the seven-degree-of-freedom full-car model is shown in Figure. 2. Table 2 summarizes all physical definitions of the full-car model with MDHPS based on a standard C-class and hatchback in Carsim software.

In Figure. 2, x_{ulf}, x_{urf}, x_{ulr}, and x_{urr} represent the displacement of unsprung mass of the left front, right front, left rear, and right rear tire, respectively; x_{slf}, x_{srf}, x_{slr}, and x_{srr} represent the displacement of sprung mass of left front, right front, left rear, and right rear tire, respectively; x_{rlf}, x_{rrf}, x_{rlr}, and x_{rrr} represent the road surface contour fluctuations of left front, right front, left rear, and right rear tire, respectively; x_{cs} represents the displacement of sprung mass; φ and θ represent the roll angle and pitch angle, respectively. The displacement symbols shown in Figure. 2 represent displacement changes relative to the initial position.

According to the principles of Newtonian mechanics and vehicle system dynamics, the seven-degree-of-freedom full car model can be presented mathematically as (11), shown at the bottom of the page, [30], where $F_{sh}(x, \dot{x})$ represents the output force shift from the force at the initial position under applied sprung mass; $\ddot{x}_{cs}$ represents the acceleration of the sprung mass. The displacement of the endpoints of the sprung mass above the four wheels can be expressed as [3]:

$$\begin{cases} x_{slf} = x_{cs} - l_a sin(\theta) - l_d sin(\varphi) \\ x_{srf} = x_{cs} - l_a sin(\theta) + l_c sin(\varphi) \\ x_{slr} = x_{cs} + l_b sin(\theta) - l_d sin(\varphi) \\ x_{srr} = x_{cs} + l_b sin(\theta) + l_c sin(\varphi) \end{cases} \tag{12}$$

Considering the attitude control of the vehicle with the proposed MDHPS can be simplified to independent adjustment of each strut, the quarter-car model will be established for controller design.

C. QUARTER-CAR MODEL

Figure. 3 illustrates the schematic diagram of the quarter-car model with MDHPS.

$$\begin{cases} m_{s\_full}\ddot{x}_{cs} = F_{sh}\left(x_{ulf} - x_{slf}, \dot{x}_{ulf} - \dot{x}_{slf}\right) + F_{sh}\left(x_{urf} - x_{srf}, \dot{x}_{urf} - \dot{x}_{srf}\right) + F_{sh}\left(x_{ulr} - x_{slr}, \dot{x}_{ulr} - \dot{x}_{slr}\right) \\ \qquad + F_{sh}\left(x_{urr} - x_{srr}, \dot{x}_{urr} - \dot{x}_{srr}\right) \\ I_{fr}\ddot{\theta} = l_a F_{sh}\left(x_{ulf} - x_{slf}, \dot{x}_{ulf} - \dot{x}_{slf}\right) + l_a F_{sh}\left(x_{urf} - x_{srf}, \dot{x}_{urf} - \dot{x}_{srf}\right) - l_b F_{sh}\left(x_{ulr} - x_{slr}, \dot{x}_{ulr} - \dot{x}_{slr}\right) \\ \qquad - l_b F_{sh}\left(x_{urr} - x_{srr}, \dot{x}_{urr} - \dot{x}_{srr}\right) \\ I_{lr}\ddot{\varphi} = l_d F_{sh}\left(x_{ulf} - x_{slf}, \dot{x}_{ulf} - \dot{x}_{slf}\right) - l_c F_{sh}\left(x_{urf} - x_{srf}, \dot{x}_{urf} - \dot{x}_{srf}\right) + l_d F_{sh}\left(x_{ulr} - x_{slr}, \dot{x}_{ulr} - \dot{x}_{slr}\right) \\ \qquad - l_c F_{sh}\left(x_{urr} - x_{srr}, \dot{x}_{urr} - \dot{x}_{srr}\right) \\ m_{ulf}\ddot{x}_{ulf} = -F_{sh}\left(x_{ulf} - x_{slf}, \dot{x}_{ulf} - \dot{x}_{slf}\right) - k_{ulf}\left(x_{ulf} - x_{rlf}\right) \\ m_{urf}\ddot{x}_{urf} = -F_{sh}\left(x_{urf} - x_{srf}, \dot{x}_{urf} - \dot{x}_{srf}\right) - k_{urf}\left(x_{urf} - x_{rrf}\right) \\ m_{ulr}\ddot{x}_{ulr} = -F_{sh}\left(x_{ulr} - x_{slr}, \dot{x}_{ulr} - \dot{x}_{slr}\right) - k_{ulr}\left(x_{ulr} - x_{rlr}\right) \\ m_{urr}\ddot{x}_{urr} = -F_{sh}\left(x_{urr} - x_{srr}, \dot{x}_{urr} - \dot{x}_{srr}\right) - k_{urr}\left(x_{urr} - x_{rrr}\right) \end{cases} \tag{11}$$

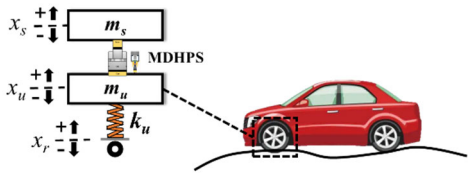

FIGURE 3. The schematic diagram of the quarter-car model with the MDHPS.

TABLE 3. Structure parameters of the quarter-car model.

Parameter	UNIT	Value
k_u	N/mm	268
m_s	kg	221
m_u	kg	54.4

TABLE 4. The gain parameters of the controller based on the z-n method.

Parameter	Value
K_p	3.78
K_i	13.40
K_d	0.15

In Figure. 3, m_s and m_u are the sprung mass and unsprung mass, respectively; x_s represents the displacement of sprung mass; x_u represents the displacement of unsprung mass; x_r represents the displacement of input excitation. The equation of motion of the quarter-car model with MDHPS can be expressed as:

$$\begin{cases} m_s\ddot{x}_s - F_{sh}\left(x_u - x_s, \dot{x}_u - \dot{x}_s\right) = 0 \\ m_u\ddot{x}_u + F_{sh}\left(x_u - x_s, \dot{x}_u - \dot{x}_s\right) + k_u\left(x_u - x_r\right) = 0 \end{cases} \tag{13}$$

Table 3 summarizes the quarter-car model parameters. The initial pre-charging pressure of gas chambers are set to 1.0MPa. The initial compression of MP (x_{ini}) can be calculated by combining with Eqs (1)-(5) and (11) as:

$$x_{ini} = [(1 - \frac{P_{GC0} + P_a}{m_s \cdot g / A_{rod} + P_a})^{(1/n)} \cdot (V_{GC0} + V_{SGC0}) - h_b \cdot A_{AGC}]/A_{rod} \tag{14}$$

IV. CONTROLLER DESIGN

In this section, the PID controller will be built and the optimal value will be identified through the Genetic Algorithm (GA) and Ziegler–Nichols (Z-N) method subjected to the quarter-car model with MDHPS.

Firstly, the gain parameters of the PID controller are defined based on the Ziegler–Nichols (Z-N) method [31], [32] under step test and summarized in Table 4.

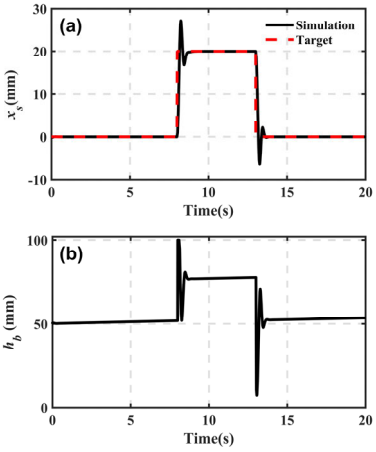

FIGURE 4. The result with PID parameters identified through the Z-N method under the positive-negative step test. (a) x_s (b) h_b.

Figure. 4 illustrates the result of x_s and the corresponding control value (h_b) with the PID controller under a positive-negative step test.

There is a large overshot of x_s shown in Figure. 4(a). To improve the adjustment performance, the values of PID parameters will be optimized using the Genetic Algorithm (GA). The boundaries are set based on the tripe of the value calculated through the Ziegler-Nichols method. The designed optimization problem is:

$$\begin{aligned} &\text{Design Values (DV) :} && K_p, K_i, \text{ and } K_d \\ &\text{Objective function :} && \text{ITAE} = \int_0^{t_s} t \cdot |e(t)| dt \\ &\text{Boundaries} && K_p(0 - 11.34); K_i(0 - 80.43); K_d(0 - 0.45) \end{aligned} \tag{15}$$

where t_s represents the simulation time; $e(t)$ is the error between the target and x_s. The Integral Time-weighted Absolute Error (ITAE) is selected as the objective function. 100 individuals are randomly generated as the initial population and the number of iterations is 100. The roulette wheel selection method is utilized to select. The probabilities of crossover and mutation are set as 60% and 1.5%, respectively. The optimization procedure is repeated at least 10 times to guarantee the convergence of the optimum. The PID parameters obtained through the optimization procedure presented in Eq. (15) have been summarized in Table 5. Figure. 5 illustrates the result and control value with modified parameters under a positive-negative step test [33].

The result shows that it can achieve the height adjustment with a smaller overshot. Figure. 6 illustrates the control block diagram of the above process.

To investigate the parameter sensitivity analysis to demonstrate the impact of these parameters on system performance [34]. The effect of the step response of PID controller with varying gains is shown in Figure 7.

TABLE 5. The modified parameters of the pid controller through genetic algorithm.

Parameter	Value
K_p	5.114
K_i	15.631
K_d	0.334

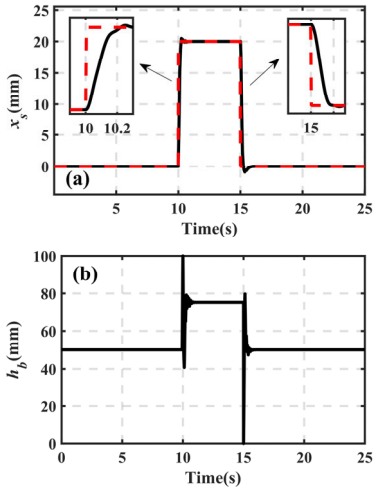

FIGURE 5. The result with PID parameters identified through the genetic algorithm under the positive-negative step test. (a) x_s (b) h_b.

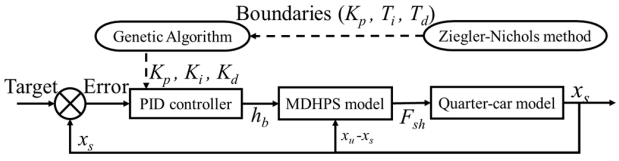

FIGURE 6. Control block diagram of the height adjustment system.

As can be observed from Figure. 7, the different values of PID parameters affect the system's performance. In Figure. 7(a), the different values of K_p affect the response speed. A higher K_p results in a larger change for a given error, which can make the system respond more quickly to disturbances. However, if K_p is set to 1.5 times the original value, it can cause the system to overshoot the setpoint and become unstable, leading to oscillations. In Figure. 7(b), K_i helps to eliminate the steady-state error, which is the difference between the desired setpoint and the actual output after the system has reached a new steady state. A higher K_i can reduce the steady-state error, but the higher value makes the system overly sensitive to noise and disturbances, potentially leading to instability. In Figure. 7(c), K_d anticipates future errors by examining the trend of the error. A higher derivative gain can help to reduce overshoot and improve stability by dampening the response, but the higher value makes the system overly sensitive to measurement noise and can cause oscillations or instability.

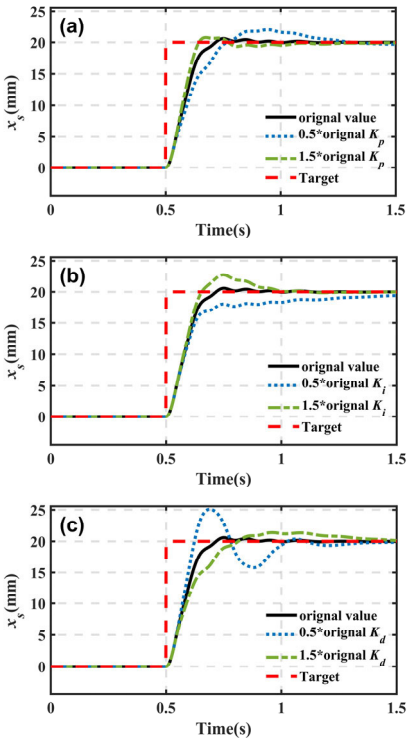

FIGURE 7. Step response of PID controller with varying gains. (a) K_p (b) K_i (c) K_d.

To verify the feasibility of the attitude control for MDHPS, the fundamental model and controller established in the previous section are combined with Carsim software and carried out in this section. The suspension's performance will be evaluated under various working conditions, such as bump excitation, acceleration, braking, and double lane-change track operation conditions. In order to verify the effectiveness of the control under the same parameters, the performance of the MDHPS with control will be compared to that without control in the following sections. The motor output characteristics are limited within the motor rating during the working process. Figure. 8 shows a block diagram of co-simulation between CarSim and Matlab/Simulink. The C-class road excitation is selected as input excitation in the Carsim software. Figure. 9 illustrates the control block diagram of a full-car system with Carsim software.

V. RESULT AND DISCUSSION

A. PITCH TEST

The road condition of speed bumps and driving operation of acceleration and brake will both cause the pitch motion and affect the stability and ride comfort of the vehicle. To evaluate the anti-pitch property, a bump excitation test and driving operation of accelerate and brake are conducted in this section.

1) BUMP EXCITATION TEST

The small bump, which is the typical road condition of the Carsim software, is used as a bump excitation test.

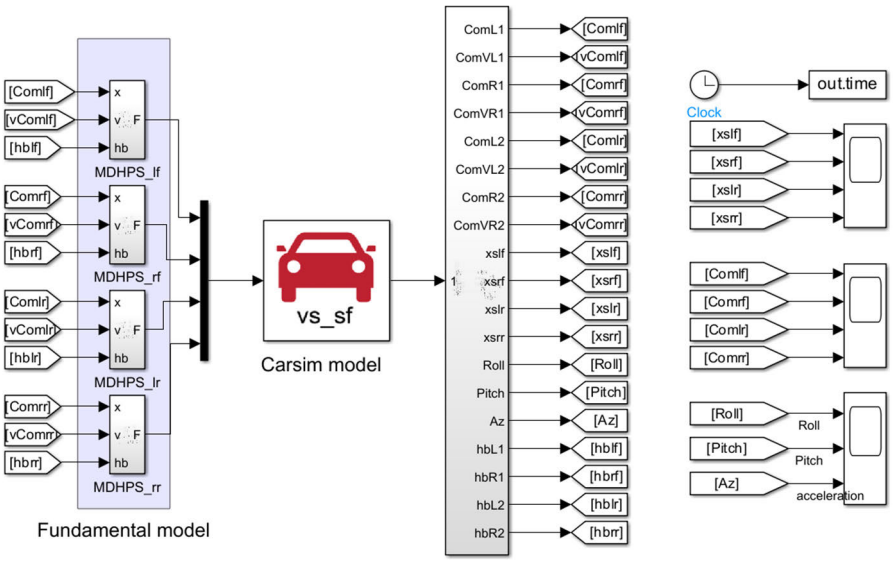

FIGURE 8. Block diagram of co-simulation between CarSim and Matlab/Simulink.

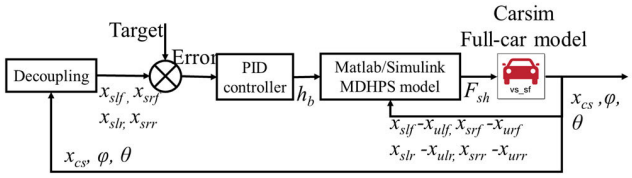

FIGURE 9. Block diagram of co-simulation between CarSim and Matlab/Simulink.

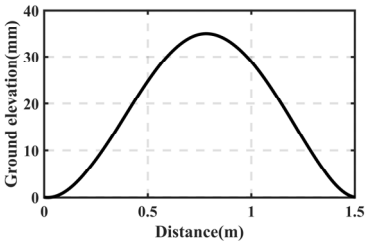

FIGURE 10. The input signal of ground elevation under bump excitation test.

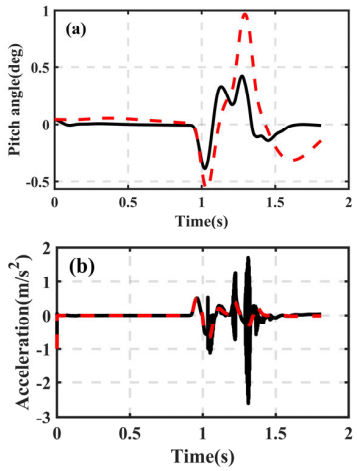

FIGURE 11. The comparison of pitch angle and car body vertical acceleration with/without control under bump excitation test. (a) pitch angle (b) car body vertical acceleration. Solid line (black) - with control; dashed line (red) - without control.

The vehicle speed is maintained at 40 km/h during testing. The ground elevation is shown in Figure. 10.

Figures. 11-15 illustrate the pitch angle, car body vertical acceleration, x_{slf}, x_{srf}, x_{slr}, x_{srr}, compression displacement, $h_{b,}$ and Dynamic Tire Load (DTL) with/without the control. Table 6 presents the maximum, minimum, and Root Mean Square (RMS) values of DTL and pitch angle.

It can be seen from Figure. 11(a) that the active control of MDHPS can provide a good anti-pitch property, in which the RMS value of pitch angle is improved by 56.24%, as shown in Table 7. It can be observed from the Figure. 11(b) that the acceleration becomes worse. The reason is that the control index of the designed controller is to minimize the strut height during working. The body acceleration will be improved in further study through the damping adjustment. As shown in Table 7, the RMS values of DTL for the front and rear tires were almost unchanged, indicating no significant difference in vehicle road adhesion. The DTL of the front and rear tire, as shown in Figure. 15 is equal to zero around 1.00s and 1.25s, which means that the vehicle has jumped due to a speed bump and stabilizes quickly. Consequently, MDHPS with active control does not affect road-holding property and it enhances the vehicle's body attitude and handling capabilities.

2) DRIVING OPERATION OF ACCELERATE AND BRAKE

The vehicle accelerates and then begins to brake after 5s. The vehicle speed and the ground elevation of the front and rear axles are shown in Figure. 16.

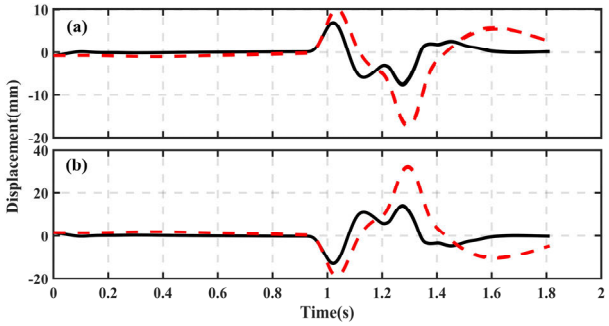

FIGURE 12. The comparison of x_s of different axles with/without control under bump excitation test. (a) front tire (b) rear tire. Solid line (black) - with control; dashed line (red) - without control.

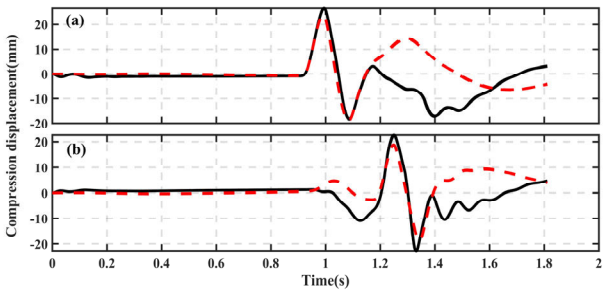

FIGURE 13. The comparison of compression displacement of different axles with/without control under bump excitation test. (a) front tire (b) rear tire. Solid line (black) - with control; dashed line (red) - without control.

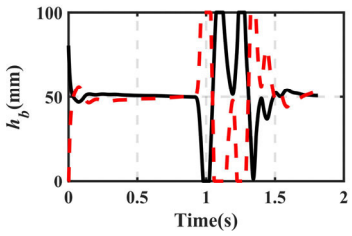

FIGURE 14. The h_b under bump excitation test. Solid line (black)-front axle; dashed line (red)-rear axle.

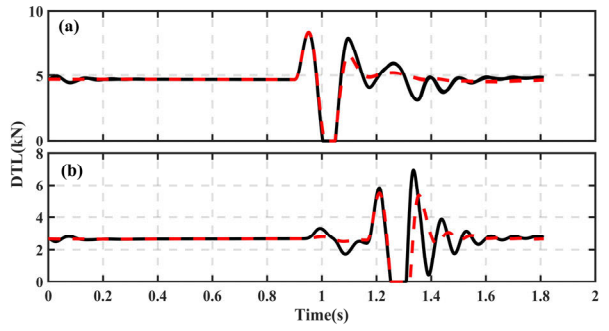

FIGURE 15. The comparison of DTL with/without controller under bump excitation test. (a) front tire (b) rear tire. Solid line (black) - with control; dashed line (red) - without control.

Figures. 17-21 illustrate the pitch angle, x_{slf}, x_{srf}, x_{slr}, x_{srr}, compression displacement, control value of $h_{b,}$ and Dynamic

TABLE 6. Comparison of maximum, minimum, and rms values for bump excitation test.

Evaluation Indicators		Passive	Active	Growth rate (%)
Pitch angle (deg)	Maximum	0.969	0.424	56.24
	Minimum	-0.564	-0.390	30.85
	RMS	0.273	0.132	51.65
DTL of front tire (KN)	Maximum	8.331	8.290	0.49
	Minimum	0	0	0
	RMS	4.790	4.820	-0.63
DTL of rear tire (KN)	Maximum	5.488	6.900	-25.73
	Minimum	0	0	0
	RMS	2.769	2.801	-1.16

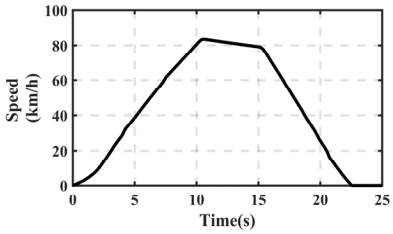

FIGURE 16. The input signal of vehicle speed under driving operation of accelerate and brake.

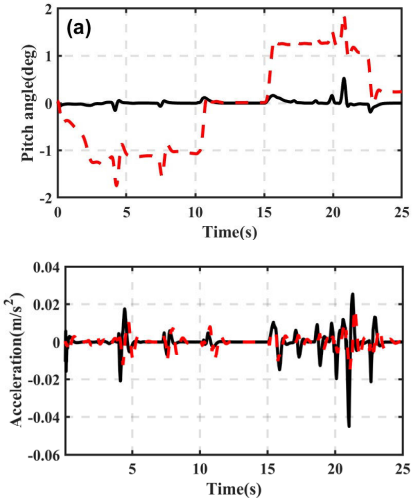

FIGURE 17. The comparison of pitch angle and car body vertical acceleration with/without control under driving operation of accelerate and brake. (a) pitch angle (b) car body vertical acceleration. Solid line (black) - with control; dashed line (red) - without control.

Tire Load (DTL) with/without the control. Table 7 presents the maximum, minimum, and Root Mean Square (RMS) values of DTL and pitch angle.

It can be seen from Figure. 17(a) that the active control of MDHPS can provide a good anti-pitch property, in which the RMS value of pitch angle is improved by 71.96%, as shown in Table 7. There is little difference in acceleration data, as shown in Figure. 17(b). As for the DTL of vehicle road adhesion shown in Table 7, the RMS values of DTL of the front tire and rear tire have no significant difference between

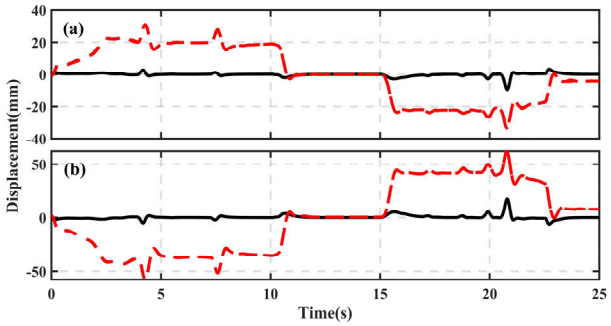

FIGURE 18. The comparison of x_s of different axles with/without control under the driving operation of accelerate and brake. (a) front tire (b) rear tire. Solid line (black) - with control; dashed line (red) - without control.

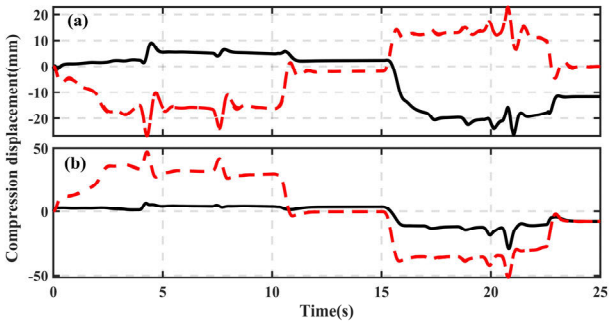

FIGURE 19. The comparison of compression displacement of different axles with/without control under driving operation of accelerate and brake. (a) front tire (b) rear tire. Solid line (black) - with control; dashed line (red) - without control.

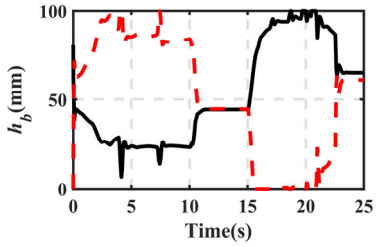

FIGURE 20. The h_b under the driving operation of accelerate and brake. Solid line (black)-front axle; dashed line (red)-rear axle.

them. Consequently, MDHPS with active control does not affect road-holding property and it enhances the vehicle's body attitude and handling capabilities.

B. ROLL TEST

In the double lane-change track operation, the vehicle is driven from one lane to another and back to the original lane according to ISO 3888-1 [35], which can evaluate the handling and anti-roll properties of the vehicle. The placing of cones for marking the double lane-change track in this test is shown in Figure. 22. In this process, the vehicle's driving speed is set to 50 km/h and 80 km/h, respectively.

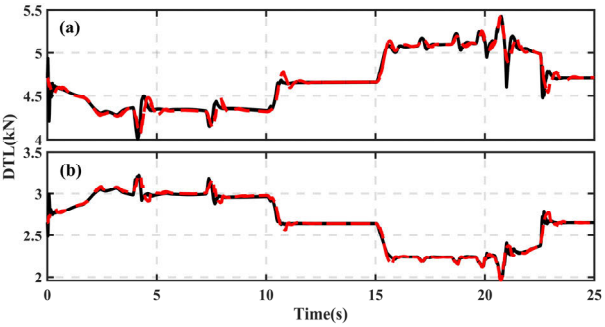

FIGURE 21. The comparison of DTL with/without controller under driving operation of accelerate and brake. (a) front tire (b) rear tire. Solid line (black) - with control; dashed line (red) - without control.

TABLE 7. Comparison of maximum, minimum, and rms values for driving operation of accelerate and brake.

Evaluation Indicators		Passive	Active	Growth rate (%)
Pitch angle (deg)	Maximum	1.872	0.525	71.96
	Minimum	-1.748	-0.190	89.13
	RMS	0.963	0.063	93.46
DTL of front tire (KN)	Maximum	5.444	5.417	0.50
	Minimum	4.085	4.010	1.84
	RMS	4.679	4.681	-0.04
DTL of rear tire (KN)	Maximum	3.227	3.219	0.25
	Minimum	1.971	1.989	-0.91
	RMS	2.684	2.680	0.15

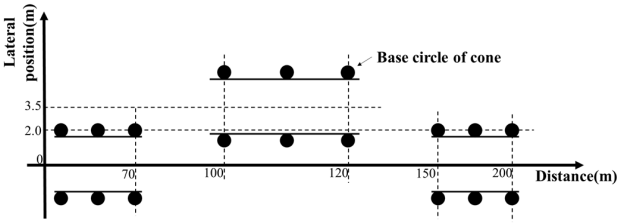

FIGURE 22. Placing of cones for marking the double lane-change track.

1) 50 km/h

Figures.23-27 illustrate the roll angle, x_{slf}, x_{srf}, x_{slr}, x_{srr}, compression displacement, $h_{b,}$ and DTL with/without the control under 50 km/h. Table 8 presents the maximum, minimum, and RMS values of roll angel and DTL.

Figure. 23 illustrates the enhanced anti-roll property of MDHPS with active control during the double lane-change maneuver. The active control has significantly improved the RMS roll angle by 79.28%, as listed in Table 8. The DTL, a key factor in vehicle road adhesion, shows negligible RMS value differences of 0.04%, 0.04%, 0.15%, and 0.15% for the left front, right front, left rear, and right rear tires in Table 8, respectively. Therefore, the active control does not deteriorate for road holding, and can greatly improve the safety and anti-roll properties, avoiding the rollover under steering conditions.

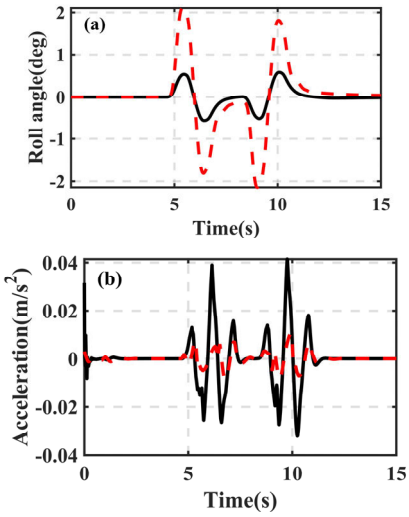

FIGURE 23. The comparison of roll angle and car body vertical acceleration with/without control under the double lane-change track test at 50 km/h. (a) roll angle (b) car body vertical acceleration. Solid line (black) - with control; dashed line (red) - without control.

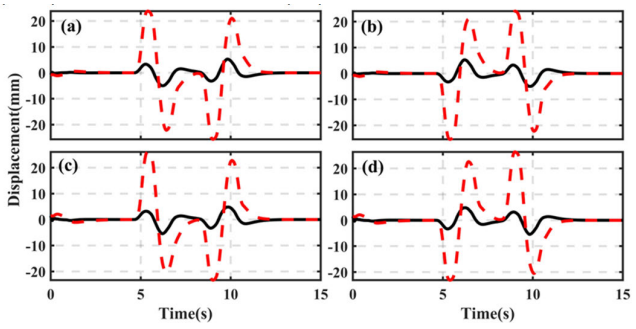

FIGURE 24. The comparison of x_s with/without control under the double lane-change track test at 50 km/h. (a) x_{slf} (b) x_{srf} (c) x_{slr} (d) x_{srr}. Solid line (black)-with control; dashed line (red)-without control.

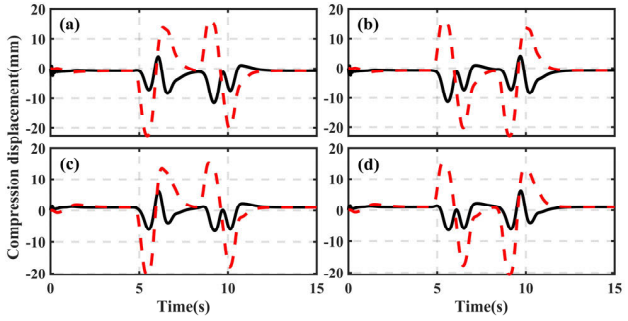

FIGURE 25. The comparison of compression displacement with/without control under the double lane-change track test at 50 km/h. (a) x_{slf} (b) x_{srf} (c) x_{slr} (d) x_{srr}. Solid line (black)-with control; dashed line (red)-without control.

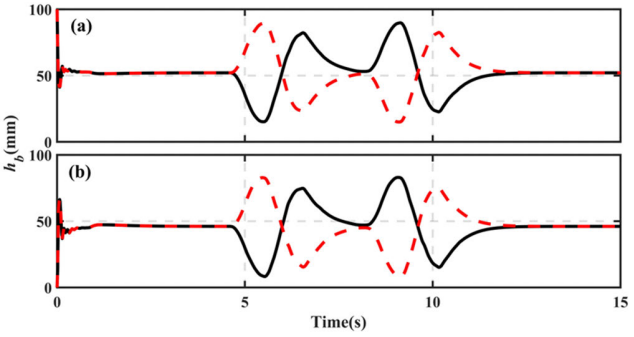

FIGURE 26. The h_b under the double lane-change track test at 50 km/h. (a) front tire (b) rear tire. Solid line (black)- left axle; dashed line (red)- right axle.

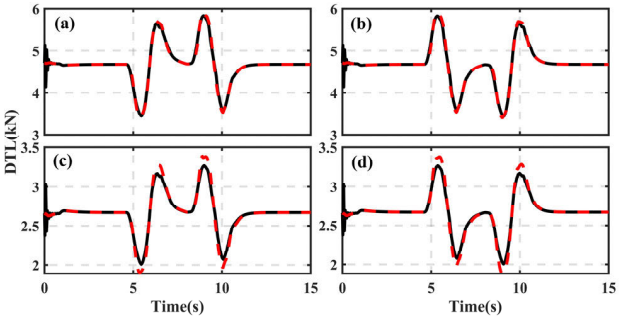

FIGURE 27. The comparison of DTL with/without control under the double lane-change track test at 50 km/h. (a) left front (b) right front (c) left rear (d) right rear. Solid line (black) - with control; dashed line (red) - without control.

TABLE 8. Comparison of maximum, minimum, and rms values for double lane-change track test at 50 km/h.

Evaluation Indicators		Passive	Active	Growth rate (%)
Roll angle (deg)	Maximum	1.684	0.349	79.28
	Minimum	-1.703	-0.351	79.39
	RMS	0.636	0.113	82.23
DTL of the left front tire (kN)	Maximum	5.918	5.833	1.44
	Minimum	3.422	3.454	-0.94
	RMS	4.694	4.692	0.04
DTL of the right front tire (kN)	Maximum	5.902	5.826	1.29
	Minimum	3.410	3.448	-1.11
	RMS	4.694	4.692	0.04
DTL of the left rear tire (kN)	Maximum	3.391	3.267	3.66
	Minimum	1.885	2.008	-6.53
	RMS	2.679	2.675	0.15
DTL of the right rear tire (kN)	Maximum	3.381	3.264	3.46
	Minimum	1.877	2.004	-6.77
	RMS	2.679	2.675	0.15

2) 80 km/h

Figures.28-32 illustrate the roll angle, x_{slf}, x_{srf}, x_{slr}, x_{srr}, compression displacement, control value of h_b, and DTL with/without the control under 50 km/h. Table 9 presents the maximum, minimum, and RMS values of roll angel and DTL.

Figure. 28 illustrates the enhanced anti-roll property of MDHPS with active control during the double lane-change maneuver. The active control has significantly improved the RMS roll angle by 50.46%, as listed in Table 9. The DTL, a key factor in vehicle road adhesion, shows negligible RMS value differences of 0.04%, 0.04%, 0.15%, and 0.15% for

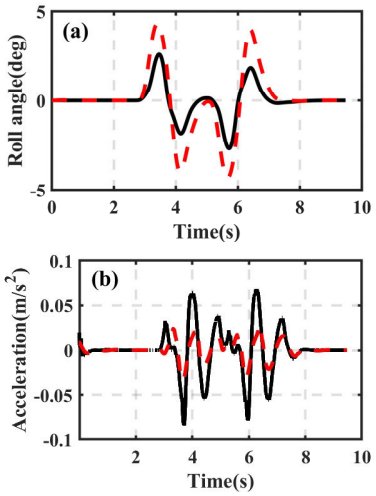

FIGURE 28. The comparison of roll angle and car body vertical acceleration with/without control under the double lane-change track test at 80 km/h. (a) roll angle (b) car body vertical acceleration. Solid line (black) - with control; dashed line (red) - without control.

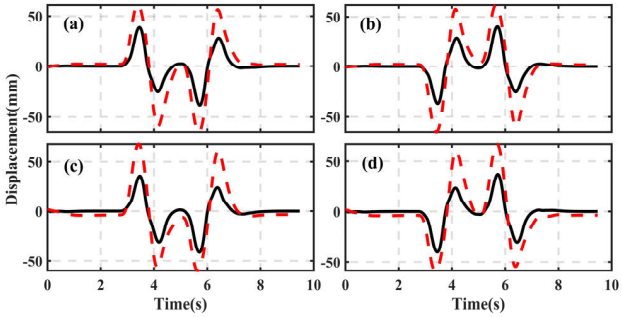

FIGURE 29. The comparison of x_s with/without control under the double lane-change track test at 80 km/h. (a) x_{slf} (b) x_{srf} (c) x_{slr} (d) x_{srr}. Solid line (black)-with control; dashed line (red)-without control.

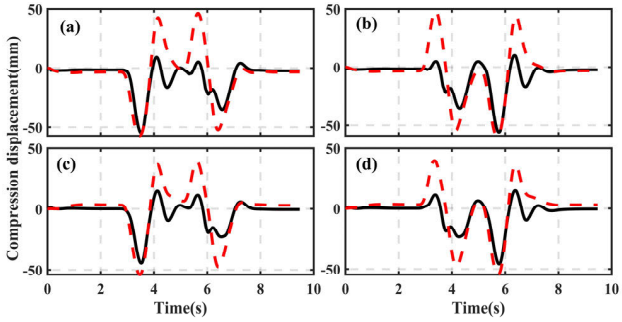

FIGURE 30. The comparison of compression displacement with/without control under the double lane-change track test at 80 km/h. (a) x_{slf} (b) x_{srf} (c) x_{slr} (d) x_{srr}. Solid line (black)-with control; dashed line (red)-without control.

the left front, right front, left rear, and right rear tires in Table 9, respectively. Therefore, the active control does not deteriorate for road holding, and can greatly improve the safety and anti-roll properties, avoiding the rollover under steering conditions.

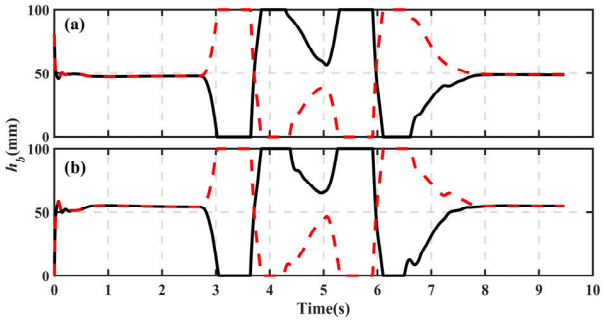

FIGURE 31. The h_b under the double lane-change track test at 80 km/h. (a) front tire (b) rear tire. Solid line (black)- left axle; dashed line (red)- right axle.

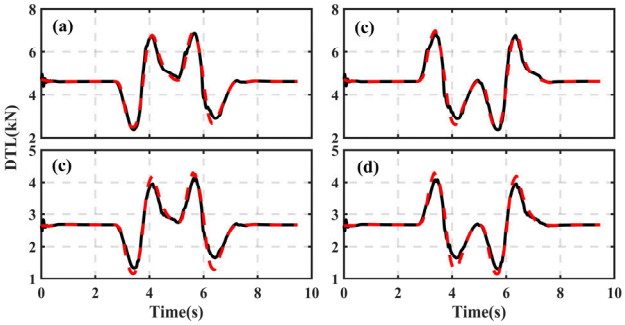

FIGURE 32. The comparison of DTL under the double lane-change track test with/without control. (a) left front (b) right front (c) left rear (d) right rear. Solid line (black) - with control; dashed line (red) - without control.

TABLE 9. Comparison of maximum, minimum, and rms values for double lane-change track test at 80 km/h.

Evaluation Indicators		Passive	Active	Growth rate (%)
Roll angle (deg)	Maximum	4.317	2.590	40.00
	Minimum	-4.331	-2.685	38.00
	RMS	1.736	0.860	50.46
DTL of the left front tire (kN)	Maximum	6.902	6.863	0.57
	Minimum	2.486	2.370	4.67
	RMS	4.710	4.708	0.04
DTL of the right front tire (kN)	Maximum	6.984	6.852	1.89
	Minimum	2.434	2.369	2.67
	RMS	4.710	4.708	0.04
DTL of the left rear tire (kN)	Maximum	4.291	4.127	3.82
	Minimum	1.163	1.329	-14.27
	RMS	2.756	2.736	0.73
DTL of the right rear tire (kN)	Maximum	4.290	4.082	4.85
	Minimum	1.154	1.303	-12.91
	RMS	2.757	2.735	0.80

VI. CONCLUSION

This paper develops a Motor-driving compacted Double-gas-chamber Hydro-Pneumatic Strut (MDHPS), which can independently achieve the height adjustment based on the constant stiffness property without change of dynamic output characteristic. It can provide a constant output characteristic during the adjustment process, which can simplify the controller design. To verify the attitude control validity of MDHPS with a simple PID controller, the optimal parameters

of the controller are identified through the Ziegler-Nichols method and Genetic Algorithm (GA) subjected to a quarter-car model. Finally, to verify the feasibility of MDHPS with a simple controller for attitude control, the full-car model is established based on the co-simulation of Carsim and Matlab/Simulink. The anti-roll and anti-pitch properties are evaluated under different working conditions, including bump excitation, acceleration, brake, and double lane-change track operation conditions. The comparison between the active and passive shows that it can greatly improve the anti-roll and anti-pitch properties with no significant difference in dynamic tire load. The improvement rate of the Root Mean Square (RMS) for both roll and pitch angles exceeds 50.46% under different working conditions.

It should be noted that the feasibility testing of attitude adjustment with MDHPS has been directly controlled by the movement of the adjusting piston (h_b) in this study. In further studies and applications, it is crucial to consider the motor's characteristic, including the acceleration and deceleration curve, correspondence of maximum velocity and torque with a lead of the lead screw. Based on the MDHPS can achieve independent attitude control, the ride comfort factors such as body acceleration will be improved through combined control with a common damping control method in further study.

ACKNOWLEDGMENT

(Ruihong Li and Bing Ma contributed equally to this work.) The authors appreciate the full support coming from Xiamen TVS Test Science and Technology Company Ltd.

REFERENCES

[1] F. Saglam and Y. S. Unlusoy, "Adaptive ride comfort and attitude control of vehicles equipped with active hydro-pneumatic suspension," *Int. J. Vehicle Design*, vol. 71, nos. 1–4, pp. 31–51, 2016, doi: 10.1504/ijvd.2016.078764.

[2] L. Wu, R. Zhou, J. Bao, G. Yang, F. Sun, F. Xu, J. Jin, Q. Zhang, W. Jiang, and X. Zhang, "Vehicle stability analysis under extreme operating conditions based on LQR control," *Sensors*, vol. 22, no. 24, p. 9791, Dec. 2022, doi: 10.3390/s22249791.

[3] Y. Yu, Z. Li, Y. Zhou, and X. Wang, "A nonlinear model predictive control for air suspension in hub motor electric vehicle," *Proc. Inst. Mech. Eng., D, J. Automobile Eng.*, early access, Jan. 2024, Art. no. 267129928, doi: 10.1177/09544070231213687.

[4] Y. Miao, X. Rui, P. Wang, H. Zhu, J. Zhang, and J. Wang, "Nonlinear dynamic modeling and analysis of magnetorheological semi-active suspension for tracked vehicles," *Appl. Math. Model.*, vol. 125, pp. 311–333, Jan. 2024, doi: 10.1016/j.apm.2023.09.027.

[5] M. Jiang, X. Rui, F. Yang, W. Zhu, H. Zhu, and W. Han, "Design and dynamic performance research of MR hydro-pneumatic spring based on multi-physics coupling model," *Nonlinear Dyn.*, vol. 111, no. 9, pp. 8191–8215, May 2023.

[6] Y. Long, X. Tan, W. Li, Y. Lai, J. Xu, and G. Wu, "Modeling and state-preview height control of electronically controlled air suspension system based on experiment," *Proc. Inst. Mech. Eng., D, J. Automobile Eng.*, vol. 238, no. 8, pp. 2465–2476, Apr. 2023.

[7] C. Liu, J. Yao, and Y. Jia, "Vehicle height control based on active suspension with permanent magnet synchronous linear motor," *Proc. Inst. Mech. Eng., D, J. Automobile Eng.*, vol. 238, no. 5, pp. 1191–1200, Dec. 2022.

[8] Q. Du, S. Chen, S. Cheng, F. Du, L. Li, Q. Li, and L. Zhang, "Suspension design and posture control for a novel by-wire chassis based on integrated electric wheel module," *J. Mech. Sci. Technol.*, vol. 36, no. 6, pp. 2669–2683, Jun. 2022, doi: 10.1007/s12206-022-0501-3.

[9] P. Karimi Eskandary, A. Khajepour, A. Wong, and M. Ansari, "Analysis and optimization of air suspension system with independent height and stiffness tuning," *Int. J. Automot. Technol.*, vol. 17, no. 5, pp. 807–816, Oct. 2016, doi: 10.1007/s12239-016-0079-9.

[10] X. Sun, Y. Cai, S. Wang, Y. Liu, and L. Chen, "Design of a hybrid model predictive controller for the vehicle height adjustment system of an electronic air suspension," *Proc. Inst. Mech. Eng., D, J. Automobile Eng.*, vol. 230, no. 11, pp. 1504–1520, Sep. 2016, doi: 10.1177/0954407015615744.

[11] C. Qiao, H. Wen, X. Liu, and G. Wang, "Damping control and experiment on active hydro-pneumatic suspension of sprayer based on genetic algorithm optimization," *Frontiers Neurorobotics*, vol. 15, Jul. 2021, Art. no. 707390.

[12] Z. Yin, A. Khajepour, D. Cao, B. Ebrahimi, and K. Guo, "A new pneumatic suspension system with independent stiffness and ride height tuning capabilities," *Vehicle Syst. Dyn.*, vol. 50, no. 12, pp. 1735–1746, Dec. 2012, doi: 10.1080/00423114.2012.660167.

[13] S. Wang, Z. Lu, X. Liu, Y. Cao, and X. Li, "Active control of hydropneumatic suspension parameters of wheel loaders based on road condition identification," *Int. J. Adv. Robotic Syst.*, vol. 15, no. 6, Nov. 2018, Art. no. 1729881418817425.

[14] X. Sun, Y. Cai, L. Chen, Y. Liu, and S. Wang, "Vehicle height and posture control of the electronic air suspension system using the hybrid system approach," *Vehicle Syst. Dyn.*, vol. 54, no. 3, pp. 328–352, Mar. 2016.

[15] R. Zhao, W. Xie, J. Zhao, P. K. Wong, and C. Silvestre, "Nonlinear ride height control of active air suspension system with output constraints and time-varying disturbances," *Sensors*, vol. 21, no. 4, p. 1539, Feb. 2021.

[16] H. Kim and H. Lee, "Height and leveling control of automotive air suspension system using sliding mode approach," *IEEE Trans. Veh. Technol.*, vol. 60, no. 5, pp. 2027–2041, Jun. 2011.

[17] R. Zhao, W. Xie, P. K. Wong, D. Cabecinhas, and C. Silvestre, "Adaptive vehicle posture and height synchronization control of active air suspension systems with multiple uncertainties," *Nonlinear Dyn.*, vol. 99, no. 3, pp. 2109–2127, Feb. 2020, doi: 10.1007/s11071-019-05412-9.

[18] S. Gp and K. Mm, "A contemporary adaptive air suspension using LQR control for passenger vehicles," *ISA Trans.*, vol. 93, pp. 244–254, Oct. 2019, doi: 10.1016/j.isatra.2019.02.031.

[19] B. Rui, "Nonlinear adaptive sliding-mode control of the electronically controlled air suspension system," *Int. J. Adv. Robotic Syst.*, vol. 16, no. 5, Sep. 2019, Art. no. 1729881419881527, doi: 10.1177/1729881419881527.

[20] X. Sun, Y. Cai, S. Wang, Y. Liu, and L. Chen, "A hybrid approach to modeling and control of vehicle height for electronically controlled air suspension," *Chin. J. Mech. Eng.*, vol. 29, no. 1, pp. 152–162, Jan. 2016, doi: 10.3901/cjme.2015.1202.141.

[21] Y. Zhou, Z. Li, W. Yu, and Y. Yu, "Cooperative control of interconnected air suspension based on model predictive control," *Appl. Sci.*, vol. 12, no. 19, p. 9886, Sep. 2022, doi: 10.3390/app12199886.

[22] R. Li, F. Yang, and D. Lin, "Design, experimental modeling and analysis of compact double-gas-chamber hydro-pneumatic strut," *Mech. Syst. Signal Process.*, vol. 172, Jun. 2022, Art. no. 109015.

[23] B. Tan, X. Lin, B. Zhang, N. Zhang, H. Qi, and M. Zheng, "Nonlinear modeling and experimental characterization of hydraulically interconnected suspension with shim pack and gas-oil emulsion," *Mech. Syst. Signal Process.*, vol. 182, Jan. 2023, Art. no. 109554, doi: 10.1016/j.ymssp.2022.109554.

[24] D. Lin, F. Yang, R. Li, and D. Gong, "Cavitation phenomenon in hydro-pneumatic interconnected suspension: Modeling and parametric analysis," *Nonlinear Dyn.*, vol. 111, no. 9, pp. 8173–8189, May 2023.

[25] H. Zhu, J. Yang, and Y. Zhang, "Dual-chamber pneumatically interconnected suspension: Modeling and theoretical analysis," *Mech. Syst. Signal Process.*, vol. 147, Jan. 2021, Art. no. 107125.

[26] S. Nie, Y. Zhuang, Y. Wang, and K. Guo, "Velocity & displacement-dependent damper: A novel passive shock absorber inspired by the semi-active control," *Mech. Syst. Signal Process.*, vol. 99, pp. 730–746, Jan. 2018, doi: 10.1016/j.ymssp.2017.07.008.

[27] D. Lin, F. Yang, D. Gong, and S. Rakheja, "Design and experimental modeling of a compact hydro-pneumatic suspension strut," *Nonlinear Dyn.*, vol. 100, no. 4, pp. 3307–3320, Jun. 2020.

[28] O. Muvengei, J. Kihiu, and B. Ikua, "Dynamic analysis of planar multibody systems with LuGre friction at differently located revolute clearance joints," *Multibody Syst. Dyn.*, vol. 28, no. 4, pp. 369–393, Nov. 2012.

[29] R. Li, F. Yang, F. Zhao, W. Zhang, and D. Lin, "Suspension height tune-up with constant stiffness properties through motor-driving double-gas-chamber hydro-pneumatic strut: Experimental study and modeling," *PLoS ONE*, vol. 19, no. 11, Nov. 2024, Art. no. e0314529, doi: 10.1371/journal.pone.0314529.
[30] H. Wang, L. Chang, and Y. Tian, "Extended state observer–based backstepping fast terminal sliding mode control for active suspension vibration," *J. Vibrat. Control*, vol. 27, nos. 19–20, pp. 2303–2318, Oct. 2021, doi: 10.1177/1077546320959521.
[31] X. Ma, P. K. Wong, J. Zhao, J.-H. Zhong, H. Ying, and X. Xu, "Design and testing of a nonlinear model predictive controller for ride height control of automotive semi-active air suspension systems," *IEEE Access*, vol. 6, pp. 63777–63793, 2018.
[32] A. B. Sharkawy, "Genetic fuzzy self-tuning PID controllers for antilock braking systems," *Eng. Appl. Artif. Intell.*, vol. 23, no. 7, pp. 1041–1052, Oct. 2010, doi: 10.1016/j.engappai.2010.06.011.
[33] T. Chen, Y. Cai, L. Chen, and X. Xu, "Sideslip angle fusion estimation method of three-axis autonomous vehicle based on composite model and adaptive cubature Kalman filter," *IEEE Trans. Transport. Electrific.*, vol. 10, no. 1, pp. 316–330, Mar. 2024.
[34] T. Chen, Y. Cai, L. Chen, and X. Xu, "Trajectory and velocity planning method of emergency rescue vehicle based on segmented three-dimensional quartic Bezier curve," *IEEE Trans. Intell. Transp. Syst.*, vol. 24, no. 3, pp. 3461–3475, Mar. 2023.
[35] *Passenger Cars Test Track for a Severe Lane-Change Manoeuvre—Part 1: Double Lane-Change*, document ISO 3888-1:2018, Dec. 2018.

RUIHONG LI was born in Xiamen, Fujian, China, in 1995. He received the B.E. (Hons.) and M.S. degrees in mechanical engineering from Huaqiao University, Xiamen, in 2018 and 2021, respectively, where he is currently pursuing the Ph.D. degree with the College of Mechanical Engineering and Automation. His research interests include vibration control and vehicle suspension.

BING MA was born in Zhumadian, Henan, China, in 1991. He received the M.S. degree in mechanical engineering from Huaqiao University, Xiamen, Fujian, China, in 2018. He is currently working with the College of Rail Transit, Henan Mechanical and Electrical Vocational College, Zhengzhou, Henan. His research interests include mechanical vibration control and new energy vehicles.

FAN YANG received the B.E. degree (Hons.) in aerospace engineering from the Civil Aviation University of China, in 1996, and the M.S. and Ph.D. degrees in mechanical engineering from Concordia University, Montreal, QC, Canada, in 2004 and 2008, respectively. He was a Postdoctoral Research Fellow and a Research Associate at Concordia University, from 2009 to 2011. He was appointed as an Associate Professor at South China University of Technology and then appointed as a Professor at Huaqiao University. He is currently working with the College of Marine Engineering, Jimei University, Xiamen, Fujian, China, where he has been working as a Professor. His research interests include mechatronics, vibration control, and the application of smart material actuators and dampers.

DEZHAO LIN was born in Zhangzhou, Fujian, China, in 1994. He received the B.E. (Hons.), M.S., and Ph.D. degrees in mechanical engineering from Huaqiao University, Xiamen, Fujian, in 2017, 2020, and 2023, respectively. Since 2023, he has been working as an Assistant Professor with the College of Marine Engineering, Jimei University, Xiamen, Fujian. His research interests include vehicle suspension, smart material, and vibration control.

WEIQIANG ZHANG was born in Quanzhou, Fujian, China, in 1996. He received the B.E. degree (Hons.) in mechanical engineering from Huaqiao University, Xiamen, Fujian, in 2019, where he is currently pursuing the master's degree with the College of Mechanical Engineering and Automation. His research interests include 4D printing of magnetic soft materials and the development of magnetic soft robots.